ACS APPLIED MATERIALS & INTERFACES

www.acsami.org

Research Article

Polymerization-Driven Self-Wrinkling on a Frozen Hydrogel Surface toward Ultra-Stretchable Polypyrrole-Based Supercapacitors

Yufeng Wang, Ying Liu, Zhengtao Wang, Dai Hai Nguyen, Chao Zhang,* and Tianxi Liu*

Cite This: *ACS Appl. Mater. Interfaces* 2022, 14, 45910−45920

Read Online

ACCESS | Metrics & More | Article Recommendations | Supporting Information

ABSTRACT: The construction of ultra-stretchable and smart supercapacitors with a large deformation-tolerance range and highly efficient self-healability is fully desired for next-generation wearable electronics. Herein, a sandwich-structured self-wrinkling hydrogel film (SSHF) is fabricated by freezing-constrained polymerization-driven self-wrinkling. Polypyrrole layers are first polymerized on a frozen pre-stretching hydrogel surface and subsequently self-wrinkled upon releasing the pre-strain. The SSHF with two polypyrrole electrode layers sandwiched with a hydrogel electrolytic layer is finally achieved by cutting four edges, and the all-in-one integrated structure creatively avoids the delamination between the electrodes and the electrolyte. The as-obtained SSHF can be directly used as an integrated all-in-one supercapacitor demonstrating high specific capacitance (79.5 F g^{-1} at 0.5 A g^{-1}), large stretchability (>500%), and reliable room temperature self-healability. The freezing-constrained polymerization-driven self-wrinkling strategy might provide a unique self-wrinkling procedure to fabricate self-healable conducting polymer-based hydrogels for ultra-stretchable smart supercapacitors.

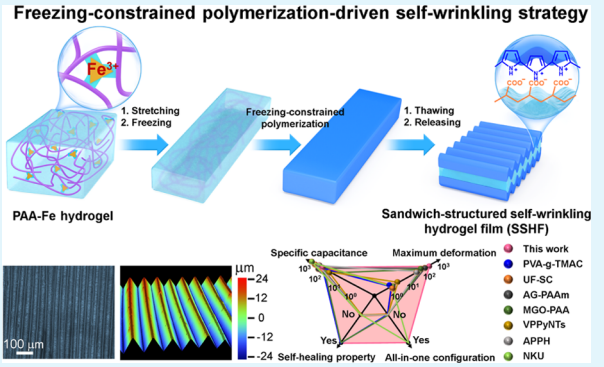

KEYWORDS: *freezing-constrained polymerization, self-wrinkling surface, stretchability, hydrogels, self-healing performance, integrated supercapacitors*

Downloaded via JIANGNAN UNIV on October 17, 2022 at 06:18:36 (UTC).
See https://pubs.acs.org/sharingguidelines for options on how to legitimately share published articles.

1. INTRODUCTION

Stretchable supercapacitors as an alternative for flexible energy storage have wide prospects in human−computer interactions, artificial intelligence, soft robotics, and other emerging fields because of their low maintenance cost, high power density, and excellent cycling performance.[1−9] Conventional flexible supercapacitors made up of rigid-featured electrode materials are difficult to meet the urgent needs of future developments of stretchable electronics. Therefore, the development of ultra-stretchable supercapacitors with high extensibility has important research and application prospects.[10] The stretchable geometric deformation structure design of stretchable supercapacitors is to build electrochemically active materials on both sides of a stretchable gel electrolyte by coating and other methods to realize the overall stretchability of the device.[11−13] However, the gel electrolyte usually has low surface energy, which makes it difficult to achieve a strong interface with the electrochemically active material on its surface, which would undoubtedly increase the interface resistance and structural instability between the electrolyte and the electrode layers.[14,15] Therefore, it is effective to build the necessary components of a supercapacitor into an all-in-one configuration through the integration strategy to solve the weak interfacial problems between the components of stretchable supercapacitors.[16] Compared with the traditional sandwich-structured supercapacitors, the integrated all-in-one supercapacitors not only have a simple assembly structure but also effectively avoid the displacement and delamination of electrochemically active materials on the surface of gel electrolytes.[17] However, due to the high stiffness and low flexibility of electrode materials, the stretchable properties of the existing all-in-one supercapacitors are limited, and the tensile range of most of these supercapacitor devices could not exceed a strain of 50%. Therefore, the development of all-in-one supercapacitors with high ductility and high energy storage performance is still facing great challenges.

Conductive polymer composite hydrogels (CPCHs) have attracted enormous attention as electrode materials for flexible supercapacitors because they could combine the high intrinsic conductivity and electrochemical activity of conductive polymers with mechanical ductility and ionic conductivity of hydrogel materials.[18−21] In addition, the conductive polymers in CPCHs usually exhibit three-dimensional continuous

Received: August 2, 2022
Accepted: September 20, 2022
Published: September 30, 2022

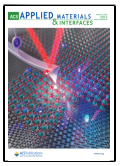

ACS Publications

© 2022 American Chemical Society

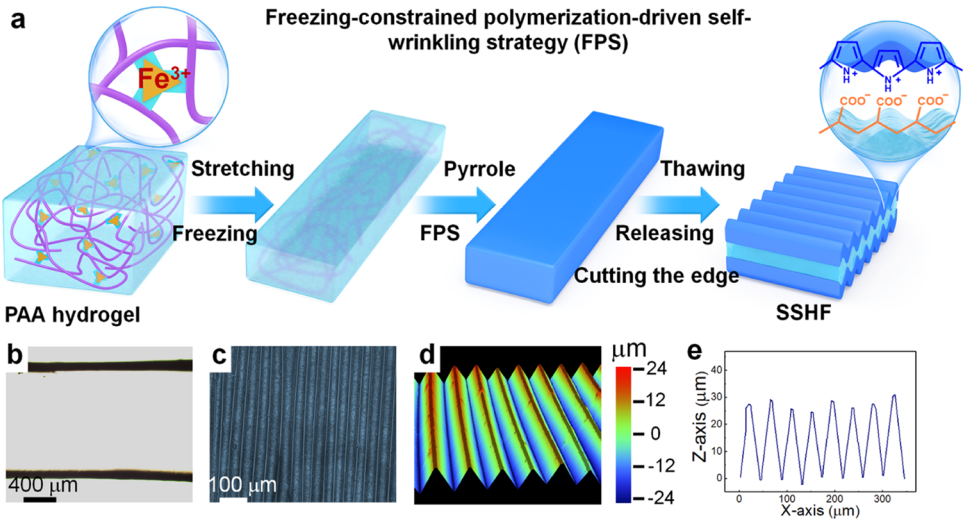

Figure 1. Fabrication and schematic of SSHFs. (a) Schematic illustration of the preparation procedure of the SSHF. (b) Cross-section and (c) top-view optical microscopy images of the SSHF. (d) 3D image and (e) height profile of the SSHF using an optical profiler.

structures in the composite hydrogels, thereby achieving a high energy density and long cycling life.[22−26] However, the use of CPCHs to build all-in-one supercapacitors requires the growth of conductive polymers on both sides of a hydrogel electrolyte film, and the growth process requires to be carefully controlled to ensure that the two conductive polymer electrode layers are not connected, avoiding possible short circuits of supercapacitor devices.[27−29] The traditional in situ growth method of conductive polymers depends on the diffusion control of the monomer concentration, and accurately controlling the growth thickness and uniformity of conductive polymers on the surface of a hydrogel electrolyte film is difficult, seriously affecting the safety and electrochemical stability of the as-prepared integrated supercapacitors.[30−32] In addition, stretchable supercapacitors usually need to face complex practical application environments, which would inevitably cause external mechanical damage to the devices. Self-healability of a supercapacitor device could effectively improve its stability, safety, and service life.[33−35] However, most of the existing self-healing supercapacitors have low self-healing efficiency and usually require additional self-healing substrates or external stimulation conditions (e.g., heating, radiation) to achieve self-healing.[36−39] Therefore, it is highly demanding while challenging to develop controllable preparation methods for fabricating conductive polymer hydrogel heterostructures for stretchable and self-healing supercapacitors.

Herein, a freezing-constrained polymerization-driven self-wrinkling (FPS) strategy is presented for preparing a sandwich-structured self-wrinkling hydrogel film (SSHF). The FPS strategy can not only achieve a hydrogel-surface constrained growth of polypyrrole (PPy) layers with precisely tailored thicknesses and areal loadings but can also boost the formation of a programmable self-wrinkling structure for realizing high stretchability. The electrostatic interactions between the in situ grown PPy layer and the hydrogel substrate are beneficial to forming stable interfaces between the electrode and electrolyte layers in the resultant supercapacitors, efficiently preventing the easy sliding of the electrode layers and the electrolyte layer. Owing to the intrinsic stretchability, unique wrinkling surface, and self-healing properties, the resultant SSHF upon the cutting of edges could be directly used as an integrated all-in-one supercapacitor with a sandwich-structured electrode−electrolyte−electrode configuration, showing high stretchability (>500% strain) and high device capacitance (79.5 F g^{-1} at 0.5 A g^{-1}). The FPS strategy might open an avenue to fabricate self-wrinkling CPCHs with great prospects in stretchable and smart energy storage.

2. MATERIALS AND METHODS

2.1. Preparation of SSHFs. The PAA-Fe hydrogel was prepared by dissolving 1 mL of acrylic acid (AA), *N*,*N*′-methylene bisacrylamide (MBAA, 0.2 wt % of AA), $FeCl_3{\cdot}6H_2O$ (5 wt % of AA), and ammonium persulfate (APS, 0.5 wt % of AA) into 4 mL of water. The mixed solution was degassed with nitrogen, poured into a poly(tetrafluoroethylene) (PTFE) mold (50 × 20 × 2 mm^3), and kept for polymerization at 70 °C for 4 h. An FPS method was used for the preparation of SSHFs using the above PAA-Fe hydrogel as a substrate. Typically, the as-obtained PAA-Fe hydrogel was pre-stretched to a certain strain (i.e., 0, 50, 100, 200, 300, 400, 500%), and then respectively immersed in liquid nitrogen while maintaining the pre-strain with clamps until completely frozen. The frozen PAA-Fe hydrogel was then immersed in a water/ethanol mixed solution (volume ratio of 1:1, pH value adjusted to 1 with HCl) with pyrrole (5 wt % of the mixed solution) and APS (equal molar amounts of pyrrole) for customized time (i.e., 1, 2, 4, 8 h) at −20 °C, for achieving space-constrained polymerization of PPy on the surface of the frozen PAA-Fe hydrogel. Upon polymerization, the above species were immersed in water and then the pre-stretching strain was released after complete thawing. Finally, the as-obtained species were washed with ethanol and water several times to remove the unreacted APS and pyrrole. A comparison sample of the PAA-Fe/PPy hydrogel was prepared using the unfrozen PAA-Fe hydrogel instead of the frozen one as the substrate while keeping other conditions similar to that of SSHFs.

2.2. Assembly of the SSHF-Based All-in-One Supercapacitors. For assembly of the SSHF-based all-in-one supercapacitors, the edges of a piece of the as-obtained SSHF were cut, and then two pieces of stainless steel current collectors were connected to the upper and lower surfaces of SSHF. The devices for electrochemical measurements were previously immersed in a 1 M KCl electrolyte solution for 12 h before testing. A conventional PPy-based supercapacitor device in an electrode−electrolyte−electrode configuration was assembled by layering two PPy films on both sides of a PAA-Fe hydrogel film (laminate-structured PPy/PAA-Fe). The PPy film was previously fabricated as follows: 0.9 g of PPy, 0.1 g of PVDF, and 2 mL of NMP were mixed into a slurry, cast on a PTFE sheet, and then dried at 80 °C for 24 h.

https://doi.org/10.1021/acsami.2c13829
ACS Appl. Mater. Interfaces 2022, 14, 45910−45920

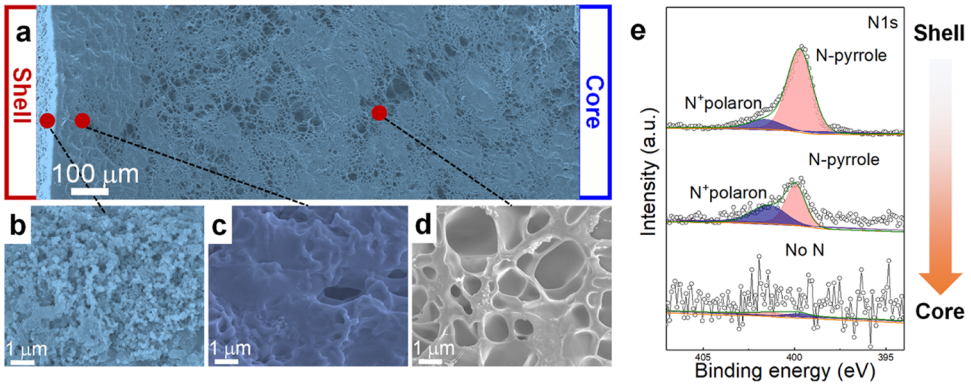

Figure 2. (a) Cross-section SEM image of the whole range of the freeze-dried SSHF, and (b–d) corresponding SEM images of various locations that are marked with filled circles in (a). (e) N 1s XPS spectra of various locations from the shell to the core within the freeze-dried SSHF.

3. RESULTS AND DISCUSSION

A representative SSHF sample was fabricated by the freezing-constrained polymerization-driven self-wrinkling (FPS) strategy. The fabrication process of the SSHF is schematically shown in Figure 1a. First, a PAA-Fe hydrogel was prepared by achieving covalent and ionic crosslinking of PAA by MBAA and Fe^{3+} ions, respectively. Second, the as-prepared PAA-Fe hydrogel was pre-stretched to a specific strain and subsequently frozen in liquid nitrogen while maintaining the pre-strain to obtain a frozen pre-stretched PAA-Fe hydrogel. The frozen hydrogel was then immersed in a water/ethanol mixed solution of pyrrole at a temperature of −20 °C. Afterward, the PPy nanoparticles were gradually in situ polymerized on the surface layer of the hydrogel through space-constrained polymerization with localized nucleation and confined polymerization of pyrrole within the boundaries between the solution and the frozen hydrogel. Finally, upon polymerization, the SSHF was obtained by thawing in water, releasing the external stress, and cutting the edges. Strong electrostatic interactions between the obtained PAA and PPy boost the formation of the stable interface and high structural stability of the resultant SSHF.

Figure 1b shows the cross-section optical microscopy image of the SSHF, exhibiting obvious sandwich-structured layers with a black opaque PPy outer layer and transparent PAA-Fe hydrogel inner layer. The formation of the sandwich-structured SSHF is related to the existence of ice crystals that limit the diffusion of pyrrole monomers into the inner layer of the PAA-Fe hydrogel to form the PPy structures on the hydrogel surface. Top-view optical microscopy image of the SSHF shows that the outer PPy has a well-organized wrinkle structure (Figure 1c). The self-wrinkling structure of SSHF was driven by the differences in the modulus of the internal soft PAA-Fe hydrogel and the stiff PPy shell. The enormous mechanical instability among the three-layer hydrogel causes self-wrinkling. Further observations of SSHF by an optical profiler (Figure 1d,e) also reveal that the wrinkling patterns exhibit highly ordered amplitude (A) and wavelength (λ).

Freeze-dried SSHF was observed by scanning electron microscopy (SEM). Figure 2a–d shows that the freeze-dried SSHF consists of diverse layers from outside to inside (cross-section of the SSHF), representing PPy (Figure 2b), PPy-PAA (Figure 2c), and PAA (Figure 2d), respectively. The outer layer of the SSHF shows a broccoli-like structure, while the inner layer of the SSHF shows a porous structure of typical freeze-dried hydrogels. EDS mappings exhibit that nitrogen is mainly distributed in the outer layer, indicating that there is almost no PPy in the inner layer (Figure S1). There exists a transition domain at the junction of the outer and inner layers, where the PPy uniformly adheres to the skeleton of the PAA-Fe hydrogel. The formation of the transition layer is related to the slow diffusion of the pyrrole monomers from the solution to the frozen hydrogel. The transition domain avoids the displacement and delamination of the as-formed multilayered structures and ensures the structural stability of the SSHF. The stress differences between the shell and core can easily cause dislocation, especially during the deformation process. In the entire SSHF, the transition layer could act as a molecular adhesive by connecting the outer and inner layers as a whole.

The interfacial interaction between the PPy and PAA was further investigated. The presence of the PAA and PPy components within the SSHF is demonstrated by Fourier transform infrared (FT-IR) spectra (Figure S2). The FT-IR spectrum of freeze-dried PAA exhibits a peak at 1698 cm^{-1}, which is assigned to the stretching band of −COOH. For the PPy, two distinct peaks that appear at 1545 and 1179 cm^{-1} are ascribed to the pyrrole ring skeletal and stretching vibrations of C−N, respectively.[40,41] Compared with the PPy and PAA, the absorption peak corresponding to the −COOH and C−N stretching vibration among the SSHF (the transition layer) shows a red-shift, indicating the formation of hydrogen bonds between the PPy and PAA. The electronic configuration and interlayer interaction of SSHF was further explored by X-ray photoelectron spectroscopy (XPS, Figure 2e). The N 1s XPS spectra of the outer layer of SSHF show two peaks at 399.4 and 401.3 eV, corresponding to the pyrrole-nitrogen and deconvoluted N^+ polaron, respectively.[42] Compared with the outer layer, the N 1s XPS spectra of the transition layer of SSHF show the proportion peak of deconvoluted N^+ polaron increasing significantly, which is attributed to the doping of PAA with the PPy skeleton. For the inner layer of SSHF, there is no obvious peak in the N 1s XPS spectra, indicating that there is no PPy in the inner layer of SSHF. The results thus confirm that the FPS strategy could achieve space-constrained polymerization of PPy, which is an effective method for preparing integrated sandwich-structured heterogeneous hydrogels. In addition, compared with the outer layer, the C−N peak in the C 1s XPS spectrum of the transition layer shows a downshift of 0.5 eV, further suggesting the formation of hydrogen bonds and electrostatic interactions between the PPy and PAA in the transition layer (Figure S3a,b). Due to the enhanced interfacial adhesion between PPy and PAA, SSHF

https://doi.org/10.1021/acsami.2c13829
ACS Appl. Mater. Interfaces 2022, 14, 45910−45920

shows a more stable microstructure than the conventional laminate-structured PPy/PAA-Fe hydrogel that is fabricated by the simple composition. Upon bath sonication of the SSHF in water, the PPy sheath did not drop off the surface for at least 10 min (Figure S4a). For comparison, upon bath sonication of laminate-structured PPy/PAA-Fe hydrogel in water, the PPy sheath easily dropped off from the hydrogel surface within 60 s (Figure S4b).

Unlike the existing CPCHs, the SSHF possesses a geometrically deformable self-wrinkling structure, which is vital to improving the stability of electromechanical properties during stretching. Amplitude and wavelength are two key parameters for evaluating the wrinkling structure, which can be adjusted by the thickness of the outer layer of the SSHF and the pre-stretching strain. SSHF-1, SSHF-2, SSHF-3, and SSHF-4 represent the PAA-Fe hydrogels maintained at −20 °C polymerizing pyrrole for 1, 2, 4, and 8 h, respectively. The cross-section optical microscopy images of SSHF-1, SSHF-2, SSHF-3, and SSHF-4 show that the thicknesses of the PPy layers in the SSHF samples are determined as 95, 158, 263, and 410 μm, respectively (Figure S5a−d). This indicates the thickness of the PPy layer in the SSHF could be adjusted by tailoring the polymerization time of pyrrole. According to the elemental analysis by a combustion method, the weight content in the SSHF samples is 3.8% (SSHF-1), 4.7% (SSHF-2), 6.1% (SSHF-3), and 9.1% (SSHF-4), respectively (Table S1). Compared with the SSHF fabricated by the FPS strategy, the PPy could uncontrollably polymerize within the PAA-Fe hydrogel when using the conventional solution-processed polymerization method. The pyrrole monomers rapidly diffuse from the solution to the hydrogel and fill the whole hydrogel in only 30 min (Figure S6a,b), indicating that the conventional solution-processed polymerization method could not constrain the polymerization of pyrrole in the outer layer of hydrogel.

The 50-SSHF, 100-SSHF, 200-SSHF, 300-SSHF, 400-SSHF, and 500-SSHF represent the PAA-Fe hydrogels which are pre-stretched to a pre-stretching strain at 50, 100, 200, 300, 400, and 500%, respectively. Figures 3a−c and S7 show a series of top-view optical microscopy images of the designed wrinkled structures of SSHF-1, SSHF-2, SSHF-3, and SSHF-4 with a pre-stretching strain at 100%, respectively. SSHF-1 exhibits relatively dense wrinkled stripes, while wrinkled stripes of SSHFs gradually become sparse with the additionally increased

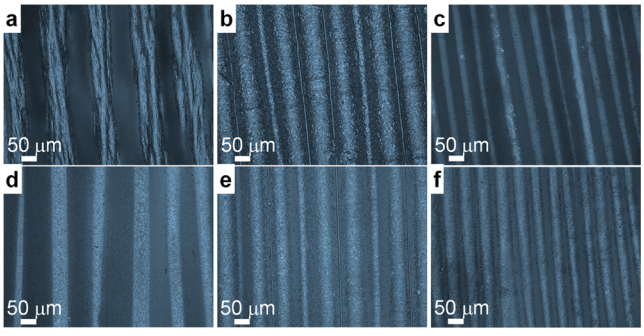

Figure 3. Morphologies of SSHFs with programmable wrinkling structures. Top-view optical microscopy images of the wrinkled structures of (a) SSHF-1, (b) SSHF-2, and (c) SSHF-3 with a pre-stretching strain at 100%. Top-view optical microscopy images of the wrinkled structures of (d) 50-SSHF, (e) 100-SSHF, and (f) 200-SSHF.

polymerization time. The density of wrinkled stripes is also related to the pre-stretching strain. With the gradually increased pre-stretching strains from 50 to 500%, the wrinkled stripes of SSHFs (polymerizing pyrrole for 2 h) vary from sparse to dense (Figures 3d−f and S8a−c). The wrinkled surface of SSHFs was further characterized using an optical profiler. Figures S9a−f and S10a−d show that the amplitudes of SSHF increase with the additionally increased polymerization time and the increased pre-stretching strains.

The amplitude and wavelength of the SSHF could be tailored by tuning the polymerization time and the pre-stretching strain of the PAA-Fe hydrogel (Figure 4a−c). The above results show that programmable wrinkle-patterned CPCHs could be prepared by the FPS strategy. When the PAA-Fe hydrogel was not pre-stretched, no wrinkle structure was formed on the surface of the hydrogel (Figure S11), due to the absence of the stress difference between the surface and inner layers.

As a result of the self-wrinkling design, the SSHF shows a stable structure and remarkable mechanical properties. The tensile stress−strain curves of the PAA-Fe hydrogel and SSHFs were measured (Figure S12a−c). The tensile stress−strain curves of the PAA-Fe hydrogel show an elastic modulus of 27.3 kPa, fracture strain of 1016%, a fracture strength of 164 kPa, and a toughness of 762.7 kJ m^{-3}. Compared with the PAA-Fe hydrogel, the SSHFs with stiff PPy exhibited a slightly enhanced elastic modulus and toughness. Taking 300-SSHF-2 as an example, its elasticity and recovery were measured by continuous loading/unloading tests. Upon conducting 1000 stretching and releasing cycles at an ultimate strain of 100%, the hysteresis curves show a slight plastic deformation of <5% (Figure S13), indicating its excellent anti-fatigue properties.

Through the incorporation of the dynamic ionic-bonded network into the composite hydrogel, the SSHF exhibits favorable self-healing ability. Figure 5a shows that SSHF-3 (pre-stretching strain at 300%) could act as a conductor in a circuit to lighten a red light-emitting diode (LED) at a voltage of 3.0 V. When the SSHF sample was cut, the LED turned off. The LED was re-lit with similar brightness when two pieces of damaged hydrogels self-healed to form a complete whole after 3 h. Even if the healing hydrogel was stretched to 200%, the LED was not extinguished, indicating that the SSHF has outstanding self-healing capability. The self-healing process of SSHF was further observed by optical micrographs (Figure S14). The crack with a 30 μm width of damaged SSHF gradually narrowed, and the cracks almost completely disappeared after healing for 3 h. It was noteworthy that the healed SSHF could withstand 200% stretching and there was no obvious crack at the interface, confirming excellent self-healability. The self-healing efficiency of SSHF was measured by tensile tests after self-healing for various specified healing times. Figure 5b shows that the strength and fracture strain of the healing SSHF restore to 94.4 and 101.9% after healing for 12 h, respectively. The rheology measurements are shown in Figures 5c and S15a,b to further confirm the self-healability of the SSHF. The storage modulus (G') of the SSHF determined by amplitude sweep rheological measurements is higher than that of the loss modulus (G'') at a small oscillatory strain (<10%), suggesting a solid-like elasticity behavior of the SSHF.[43] With the increase of oscillatory strain, the G' begins to decrease and G'' is higher than G' (>500%), indicating that the network of the SSHF was destroyed under large deformation (Figure S15a). Frequency-sweep rheological

https://doi.org/10.1021/acsami.2c13829
ACS Appl. Mater. Interfaces 2022, 14, 45910−45920

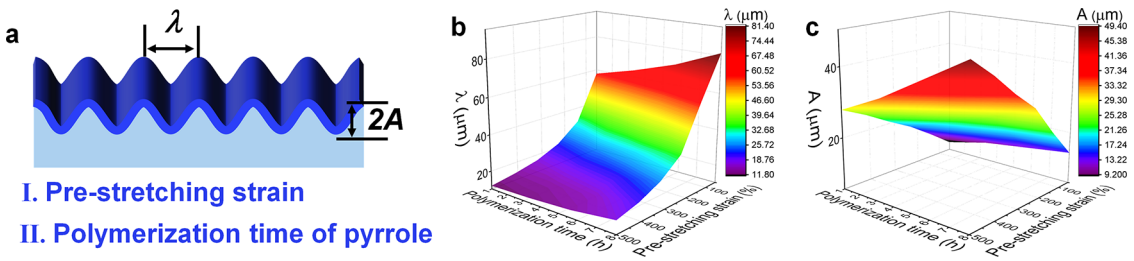

Figure 4. (a) Schematic diagram of the SSHFs with designed wrinkling surfaces. Regulations of (b) wavelength and (c) amplitude of SSHFs by tailoring the polymerization time and the pre-stretching strain, respectively.

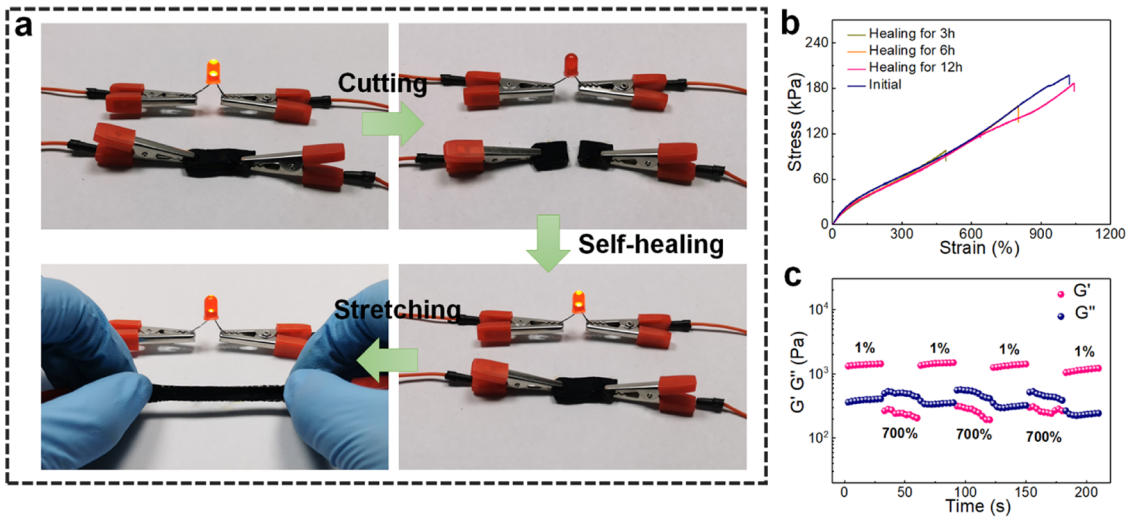

Figure 5. Self-healing performances of SSHFs. (a) Digital photos showing an SSHF sample connected into a circuit lightening up a red LED upon cutting, self-healing, and further stretching. (b) Tensile stress−strain curves of the damaged SSHF after self-healing for various time. (c) Step-strain sweep test of the SSHF with alternating shear strains of 1 and 700%.

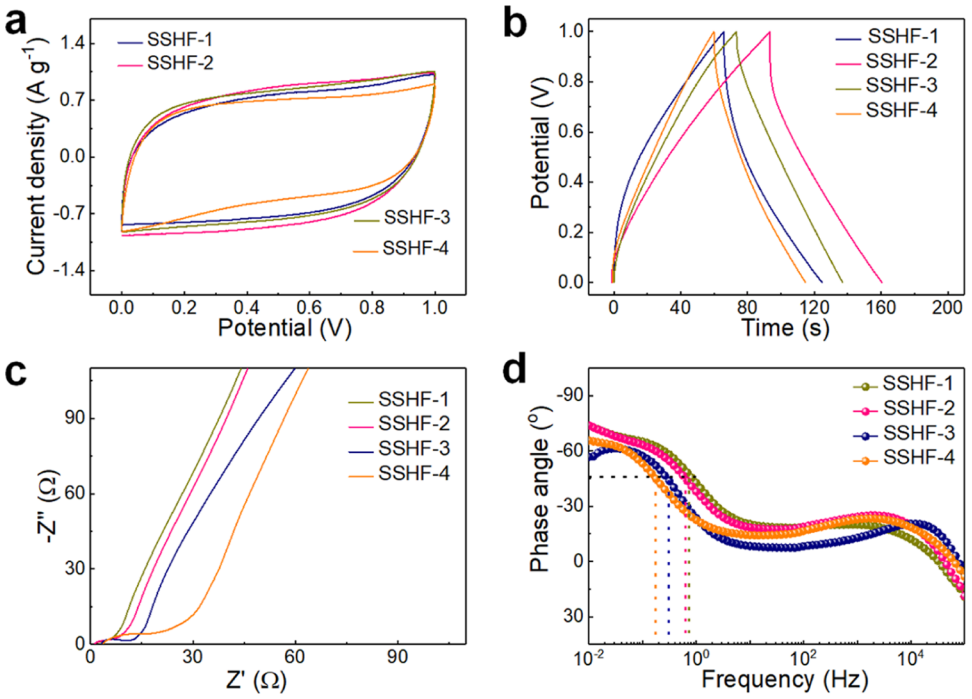

Figure 6. Electrochemical performances of SSHFs. (a) CV curves at 10 mV s^{-1}, (b) GCD curves at 1 A g^{-1}, (c) Nyquist plots, (d) Bode plots of SSHF-1, SSHF-2, SSHF-3, and SSHF-4.

https://doi.org/10.1021/acsami.2c13829
ACS Appl. Mater. Interfaces 2022, 14, 45910−45920

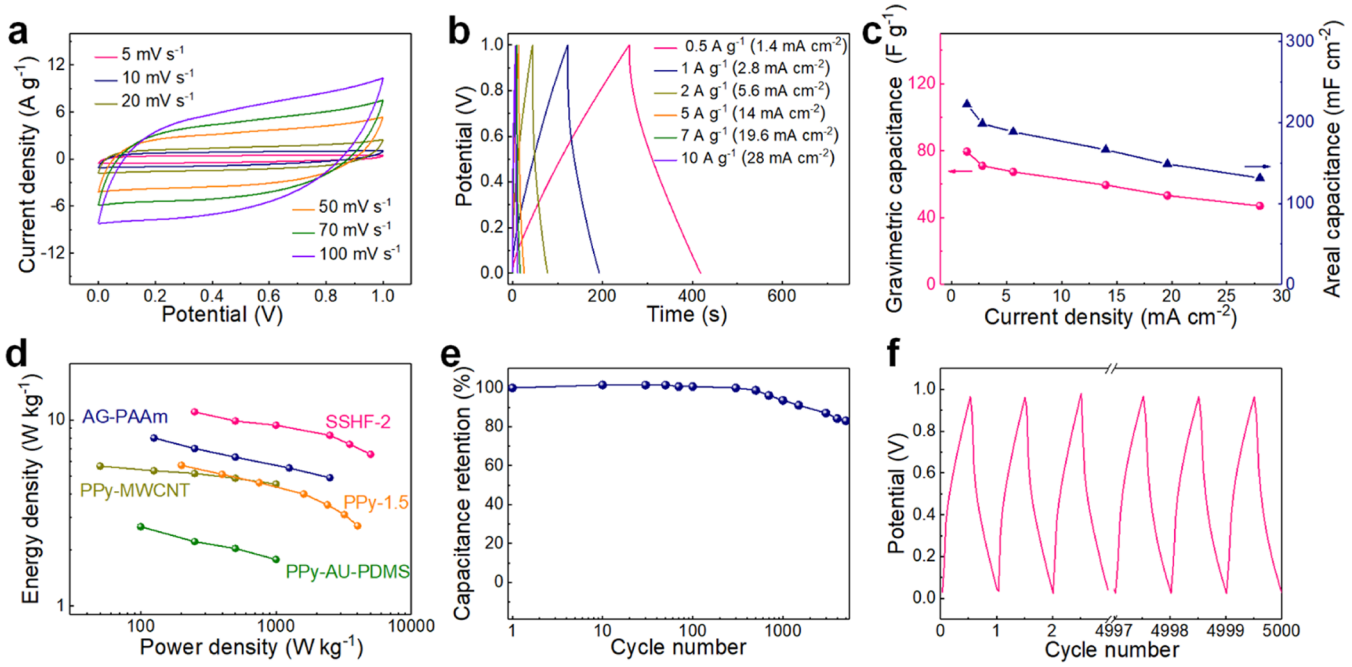

Figure 7. (a) CV curves of SSHF-2 at various scan rates. (b) GCD curves of SSHF-2 at various current densities. (c) Areal and gravimetric capacitances of SSHF-2 at various current densities. (d) Ragone plots of SSHF-2 in comparison to PPy-based flexible supercapacitors in the literature. (e) Cycling performance of SSHF-2 for 5000 cycles. (f) GCD curves of SSHF-2 in the first and last three cycles.

measurements of the SSHF show that the G' is higher than G'' at an angular frequency (ω) ranging from 1 to 100 rad s^{-1} (Figure S15b), indicating the stable network structure of SSHF in the entire frequency range. Cyclic step-amplitude sweep tests with alternate small-strain (1%) and large-strain (700%) oscillatory were performed (Figure 5c). At the oscillatory strain of 1%, the G' is larger than G''. However, G' exhibits a sharp decline that is lower than G'' when the oscillatory strain switches to 700%. Subsequently, the G' and G'' of SSHF immediately return to the initial values when the oscillatory strain switches to 1% again and this process could be repeated four times without any apparent loss in G' and G'', suggesting the rapid and repeatable self-healability of SSHF.

Electrochemical properties of the SSHF as a stretchable integrated supercapacitor were measured in detail by cyclic voltammetry (CV) curves, galvanostatic charge/discharge (GCD) tests, and electrochemical impedance spectroscopy (EIS). The CV curves of the SSHF (at a scan rate of 10 mV s^{-1}) with various polymerization times of pyrrole show that SSHF-2 has the largest area surrounded by CV curves, followed by SSHF-3, SSHF-1, and SSHF-4 (Figure 6a), indicating the highest special capacitance of SSHF-2. No redox peaks were found in the CV curves of all SSHF samples. The SSHF supercapacitor is assembled in a symmetrical two-electrode system, and the voltage applied to the SSHF is the potential difference between two electrodes with an equal voltage value at each electrode. During the CV measurements, the redox reaction takes place at both electrodes, one being reduced and the other oxidized. The currents that are collected are the sum of the two electrodes.[44] Therefore, it is difficult to record the redox peaks in the CV test of the SSHF. The results of GCD (at a current density of 1 A g^{-1}) are consistent with CV (Figure 6b), that is, SSHF-2 shows the longest discharge time.

The electrochemical performance of the SSHF was further investigated by EIS (Figure 6c), and test results were fitted using an equivalent circuit (Figure S16). The low-, mid-, and high-frequency regions of the Nyquist plots correspond to the capacitive behavior, the diffusion-limited electrode process, and the electron-transfer limited process, respectively. In the high-frequency range, the electrode−electrolyte interface charge transfer behavior is represented by semicircles in the Nyquist plots.[45−47] Notably, the distorted semicircular arc is attributed to the overlapping of the mid-frequency diffusing effect and high-frequency redox reaction due to the 3D porous structure of the SSHF. The intersection of curves and real axis in the Nyquist plots reflect the equivalent series resistance (R_s) for the whole electrochemical system, which comprises the electrode resistance, solvent resistance, and the interface resistance between the current collector and electrode. Compared with SSHF-1, SSHF-3, and SSHF-4, SSHF-2 exhibits the smallest R_s (Table S2). In the low-frequency range, the Nyquist plots show that SSHF-1 and SSHF-2 have steeper slopes than that of SSHF-3 and SSHF-4, suggesting fast ion diffusion rates of SSHF-1 and SSHF-2. Moreover, the Bode plots of the SSHF supercapacitors show that SSHF-4 has the largest RC time constant (5.8 s, Figure 6d) among the supercapacitors, which further confirms the sluggish ion diffusion kinetics of SSHF-4. The sluggish ion diffusion kinetics of SSHF-4 are attributed to the thick PPy layer blocking the ion diffusion. Consequently, the smallest R_s and excellent ion diffusion of the SSHF-2 supercapacitor endows it with an optimized energy storage performance among SSHFs.

The electrochemical performance of SSHF-2 was further evaluated by CV curves at different scan rates. Figure 7a shows that the CV curves of SSHF-2 exhibit a similar quasi-rectangular shape with the increase of the scan rate (from 5 to 100 mV s^{-1}), implying that SSHF-2 owns excellent capacitive behavior. The symmetric shape GCD curves (current density from 0.5 to 10 A g^{-1}) further confirm that SSHF-2 possesses reversible charge−discharge behavior (Figure 7b). The areal and gravimetric capacitances of the

https://doi.org/10.1021/acsami.2c13829
ACS Appl. Mater. Interfaces 2022, 14, 45910−45920

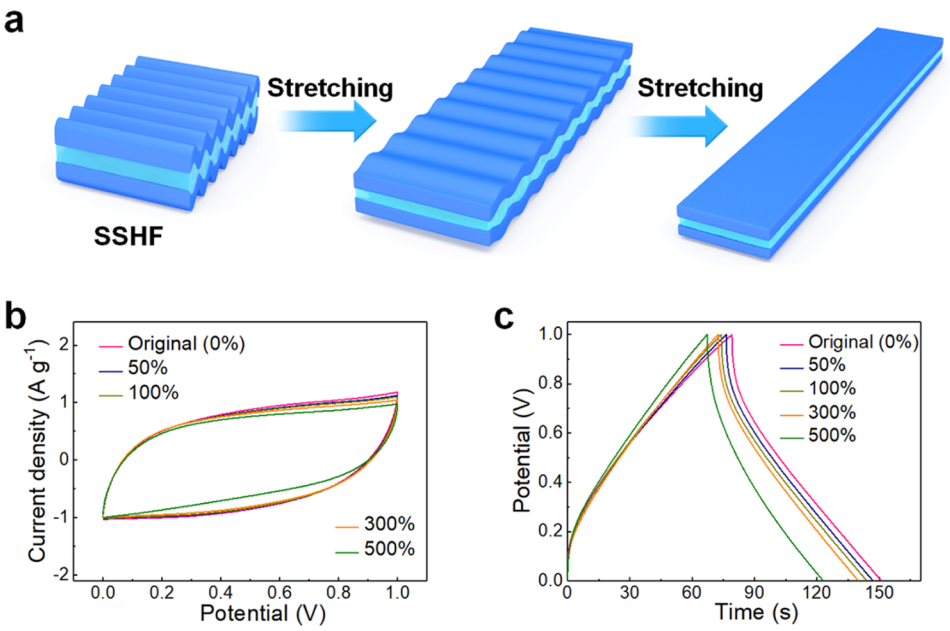

Figure 8. Deformation-tolerant properties of the SSHF supercapacitors. (a) Schematic of the SSHF during stretching. (b) CV and (c) GCD curves of the SSHF-2 supercapacitor in its initial and stretching states.

SSHF-2 supercapacitor under various current densities are calculated according to the GCD curves (Figure 7c). The specific gravimetric and areal capacitance of the SSHF-2 supercapacitor was calculated to be 79.5 F g^{-1} (at a current density of 0.5 A g^{-1}) and 222.6 mF cm^{-2} (at a current density of 1.4 mA cm^{-2}), respectively. The specific gravimetric and areal capacitance of the SSHF-2 supercapacitor are maintained at 59.5 F g^{-1} and 166.6 mF cm^{-2}, respectively, when the current density increases from 0.5 to 5 A g^{-1} (1.4−14 mA cm^{-2}), indicating its excellent rate capability.

Figure 7d shows the Ragone plots of SSHF-2 in comparison with previously reported results of PPy-based flexible supercapacitors. SSHF-2 demonstrates a superior energy density of 11.04 Wh kg^{-1} (power density of 0.25 kW kg^{-1}) to that of the previously reported PPy-based flexible supercapacitors. Moreover, the stretchable integrated SSHF-2 supercapacitor also shows excellent cycling stability. After 5000 charge−discharge cycles, the special capacitance of the SSHF-2 supercapacitor is retained at more than 83.1% at a current density of 5 A g^{-1} (Figure 7e,f), and the slight decreases in special capacitance are due to the expansion and contraction of the PPy electrode material during cycling. The remarkable capacitance and stable cyclic performance of SSHF-2 are attributed to its unique structural design. The integrated structure of SSHF-2 optimizes the transportation of electrons and charges, and greatly reduces the interface contact resistance between the electrodes and electrolytes. To prove this, the influence of the preparation methods of composite hydrogels on the electrochemical performance was explored by comparing SSHF-2 (by the FPS process) and the laminate-structured PPy/PAA-Fe (by the lamination process). Figure S17a shows that the area surrounded by the CV curve (at a scan rate of 10 mV s^{-1}) of SSHF-2 is significantly larger than that of laminate-structured PPy/PAA-Fe. The GCD curves also show that SSHF-2 has a longer discharge time than the laminate-structured PPy/PAA-Fe (Figure S17b). The corresponding EIS curves indicate that SSHF exhibits optimized ion diffusion and charge transfer behaviors (Figure S17c), which was proved by the smaller RC time and R_s (Table S2), respectively. The above results are attributed to the integrated structure of SSHF-2, which greatly reduces the impedance between the interfaces and optimizes the ion diffusion paths.

Benefiting from the SSHF with high ionic conductivity, stretchability, and self-healable properties, the SSHF-based supercapacitor could be used as a potential energy storage device for complex application scenarios. As previously mentioned, a stretchable supercapacitor was fabricated by the FPS strategy (Figure 8a), and the pre-stretching strain is the main factor affecting the deformable range of the supercapacitor. Figure 8b shows that the CV curves of SSHF-2 (pre-stretching strain at 500%) remain similar in quasi-rectangular shape even under high tensile strain. Notably, the almost overlapping CV curves as the tensile strain are less than 300% indicating that the supercapacitor device has stable electrochemical performance under stretching. As the SSHF-2 supercapacitor was further stretched to 500%, the reduced area of CV curves was attributed to significantly increased series resistance. The results are also demonstrated by the GCD curves (Figure 8c).

In situ optical microscopy was used to study the evolution of the surface pattern of SSHF during tensile deformation. Taking SSHF-2 (pre-stretching strain at 300%) as an example, it showed a uniform wrinkled structure (Figure 9a−f). The wrinkle pattern of SSHF-2 in the field of view was sparse as the tensile strain increased (stretch along the corrugation direction), indicating that the wrinkling intervals of SSHF-2 increased during stretching. During the whole stretching process, the structure of the PPy layer was not damaged. Notably, when SSHF-2 was stretched to 300% (tensile strain is equal to pre-stretching strain), the wrinkle pattern almost completely disappeared and the orientation stripes appeared in the stretch direction, indicating that the PPy of the surface layer began to be stretched. The results fully demonstrate that rigid PPy can achieve large tensile deformation (the maximum deformable range is around pre-stretching strain) by the geometric deformation of the wrinkle structure. The unique

https://doi.org/10.1021/acsami.2c13829
ACS Appl. Mater. Interfaces 2022, 14, 45910−45920

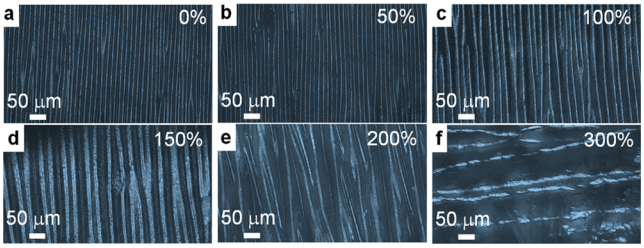

Figure 9. Top-view optical images of SSHF-2 (300% pre-stretching strain) during (a) 0%, (b) 50%, (c) 100%, (d) 150%, (e) 200%, and (f) 300% stretching.

morphological evolution of SSHF enabled the supercapacitor to keep good energy storage performance in stretching. In addition, even after 1000 stretching cycles (100% tensile strain), the CV curves of SSHF-2 also retained a quasi-rectangular shape similar to its original state (Figure S18), further indicating the excellent stretchability of the SSHF-2 supercapacitor.

In addition to stretchability, the supercapacitor allows the self-healability of the SSHF to be retained, which is conducive to improving the safety and durability of the device. The CV curve of SSHF-2 almost overlapped with the initial state after 7 cutting-healing cycles, indicating excellent self-healing performance (Figure 10a). The GCD curves showed the discharge time of the device after healing was similar to that of the initial state, which further confirmed that the electrochemical performance of the supercapacitor had been repaired (Figure 10b). The corresponding EIS curves also exhibited similar ion diffusion and charge transfer behaviors, indicating that the electrical properties of SSHF had been recovered (Figure S19).

Compared with the current flexible supercapacitors,[6,15,29,31,48−50] the SSHF shows extraordinary electromechanical versatility in terms of autonomous self-healing, high stretchability, high specific capacitance, and all-in-one structure (Figure 10c, Table S3). In addition, the SSHF also shows high healing efficiency and a fast self-healing rate compared with previously reported self-healable elastomers (Table S3). Assembly of supercapacitors in parallel and/or series is an effective way to meet various working-voltage and discharging capacity requirements for practical applications. As a proof of concept, the four units of SSHF-2 supercapacitors that were connected in parallel increased the discharge capacity, while four units connected in series enlarged the total output voltage. CV and GCD measurements demonstrated that the output voltage of four supercapacitor units in series was 4-fold that of a single unit, and the discharging capacity of the four supercapacitor units in parallel was 4-fold that of a single unit (Figure 10d,e). As a demonstration, four devices were connected in series to light up a red light-emitting diode (LED) during 200% stretching (Figure 10f), indicating stable energy storage performance under deformation.

4. CONCLUSIONS

In summary, a sandwich-structured self-wrinkling hydrogel film (SSHF) with highly ordered and controllable wrinkling surface patterns was fabricated by the freezing-constrained polymerization-driven self-wrinkling (FPS) strategy. The developed FPS strategy using ice crystals could limit the diffusion of pyrrole monomers into the inner layer of the PAA-Fe hydrogel and realize space-constrained growth of PPy on the hydrogel surface. The integrated core−shell heterogeneous design of the resultant SSHF with strong electrostatic interactions between the PPy layer and the PAA core greatly improves the structural stability between the PPy electrode layers and the PAA electrolyte layer, avoiding the easy shedding and sliding of PPy layers from the all-in-one supercapacitor device. The unfolding of the self-wrinkled structures of SSHF is beneficial for achieving high structural stability of PPy electrode layers under large tensile strain. The SSHF also exhibits a favorable self-healability at room temperature, allowing the sandwich-structured hydrogel to spontaneously heal mechanical/electrical properties when damaged. As a stretchable super-

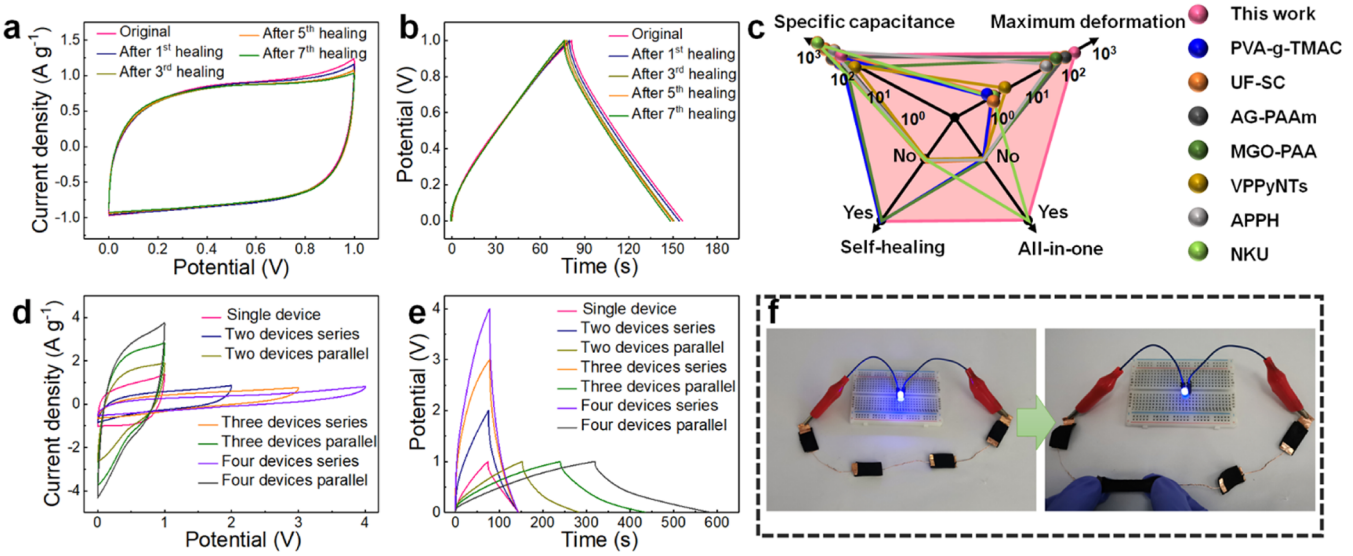

Figure 10. (a) CV curves at 10 mV s^{-1} and (b) GCD curves at 1 A g^{-1} of SSHF-2 (500% pre-stretching strain) for various cutting/healing cycles. (c) Comparison between the SSHF and other flexible supercapacitors in the literature in terms of self-healability, all-in-one structure, maximum deformation, and specific capacitance. (d) CV curves at 10 mV s^{-1}, and (e) GCD curves at 1 A g^{-1} of one, two, three, and four SSHF-2 (500% pre-stretching strain) connected in series and parallel. (f) Digital photographs of an integrated device with four series-connected SSHFs lighting up an LED and then one device being stretched to 200% strain.

https://doi.org/10.1021/acsami.2c13829
ACS Appl. Mater. Interfaces 2022, 14, 45910−45920

capacitor, the all-in-one design of electrodes and electrolytes simplifies the assembling process and effectively reduces the contact resistance of the device. As a result, the SSHF-based all-in-one supercapacitor shows high energy storage (up to 79.5 F g^{-1} at a current density of 0.5 A g^{-1}), large stretchability (>500%), and reliable self-healing performance. This study not only provides a novel synthetic method for fabricating a highly stretchable, self-healable, and self-wrinkling CPCH with an integrated all-in-one sandwich-structured configuration but also inspires a new avenue for the development of ultra-stretchable and self-healable supercapacitors for wearable electronics.

■ ASSOCIATED CONTENT

Supporting Information

The Supporting Information is available free of charge at https://pubs.acs.org/doi/10.1021/acsami.2c13829.

Materials; characterizations; SEM image, EDS mappings of freeze-dried SSHFs; FT-IR spectra of freeze-dried PAA-Fe, PPy, and SSHFs; C 1s XPS spectra of outer layer, transition layer sections from freeze-dried SSHFs; digital photos of SSHFs upon sonication; digital photos of the laminate-structured PPy/PAA-Fe hydrogel upon sonication; cross-section optical microscopy images of SSHFs, PAA-Fe/PPy hydrogel by conventional solution-processed polymerization; top-view optical microscopy images of the designed wrinkled structures of SSHF-4; top-view optical microscopy images of the designed wrinkled structures of SSHFs; top-view optical microscopy images of SSHFs using an optical profiler with a polymerization time for 2 h and the pre-stretching strain of 100%; top-view optical microscopy images of SSHFs without pre-stretching; tensile curves, tensile strength and elastic modulus, fracture strain and toughness of the PAA-Fe hydrogel and SSHFs; tensile fatigue test of SSHF-2 with 100% strain for 1000 cycles; optical microscopy images of the self-healing process of SSHFs; amplitude sweep rheological measurement of SSHFs from 0.1 to 1000%; frequency-sweep rheological measurement of SSHFs from 1 to 100 rad s^{-1}; equivalent circuit diagram of SSHF supercapacitors; CV curves, GCD curves, and Nyquist plots of SSHF-2 and laminate-structured PPy/PAA-Fe; CV curves of SSHF-2 after 1000 stretching/releasing cycles; Nyquist plot of SSHF-2 after 7-time cutting and self-healing cycles; table summarizing elemental analysis of freeze-dried SSHF; table summarizing R_s and RC time constants of SSHFs and the laminate-structured PPy/PAA-Fe hydrogel; table summarizing the comparison of the SSHF supercapacitor with previously reported flexible supercapacitors or self-healing elastomers in terms of maximum deformation, self-healability, and specific capacitance (PDF)

■ AUTHOR INFORMATION

Corresponding Authors

Chao Zhang − *State Key Laboratory for Modification of Chemical Fibers and Polymer Materials, College of Materials Science and Engineering, Donghua University, Shanghai 201620, P. R. China;* orcid.org/0000-0003-1255-7183; Email: czhang@dhu.edu.cn

Tianxi Liu − *State Key Laboratory for Modification of Chemical Fibers and Polymer Materials, College of Materials Science and Engineering, Donghua University, Shanghai 201620, P. R. China; Key Laboratory of Synthetic and Biological Colloids, Ministry of Education, School of Chemical and Material Engineering, Jiangnan University, Wuxi 214122, P. R. China;* orcid.org/0000-0002-5592-7386; Email: txliu@jiangnan.edu.cn

Authors

Yufeng Wang − *State Key Laboratory for Modification of Chemical Fibers and Polymer Materials, College of Materials Science and Engineering, Donghua University, Shanghai 201620, P. R. China*

Ying Liu − *State Key Laboratory for Modification of Chemical Fibers and Polymer Materials, College of Materials Science and Engineering, Donghua University, Shanghai 201620, P. R. China;* orcid.org/0000-0001-6970-4469

Zhengtao Wang − *State Key Laboratory for Modification of Chemical Fibers and Polymer Materials, College of Materials Science and Engineering, Donghua University, Shanghai 201620, P. R. China*

Dai Hai Nguyen − *Institute of Applied Materials Science, Vietnam Academy of Science and Technology, Ho Chi Minh City 800010, Vietnam;* orcid.org/0000-0003-3501-7390

Complete contact information is available at: https://pubs.acs.org/10.1021/acsami.2c13829

Author Contributions

This manuscript was written with the contributions of all the authors. All authors have approved the final version of the manuscript.

Notes

The authors declare no competing financial interest.

■ ACKNOWLEDGMENTS

This work was financially supported by the National Natural Science Foundation of China (21875033 and 52122303) and the Shanghai Scientific and Technological Innovation Project (22520714500).

■ REFERENCES

(1) Vaghasiya, J. V.; Mayorga-Martinez, C. C.; Pumera, M. Flexible Energy Generation and Storage Devices: Focus on Key Role of Heterocyclic Solid-State Organic Ionic Conductors. *Chem. Soc. Rev.* **2020**, *49*, 7819−7844.

(2) Liu, H.; Zhang, H.; Han, W.; Lin, H.; Li, R.; Zhu, J.; Huang, W. 3d Printed Flexible Strain Sensors: From Printing to Devices and Signals. *Adv. Mater.* **2021**, *33*, No. 2004782.

(3) Zhu, M.; Ji, S.; Luo, Y.; Zhang, F.; Liu, Z.; Wang, C.; Lv, Z.; Jiang, Y.; Wang, M.; Cui, Z.; Li, G.; Jiang, L.; Liu, Z.; Chen, X. A Mechanically Interlocking Strategy Based on Conductive Microbridges for Stretchable Electronics. *Adv. Mater.* **2022**, *34*, No. 2101339.

(4) Zhang, G.; Hu, J.; Nie, Y.; Zhao, Y.; Wang, L.; Li, Y.; Liu, H.; Tang, L.; Zhang, X.; Li, D.; Sun, L.; Duan, H. Integrating Flexible Ultralight 3d Ni Micromesh Current Collector with Nico Bimetallic Hydroxide for Smart Hybrid Supercapacitors. *Adv. Funct. Mater.* **2021**, *31*, No. 2100290.

(5) Sajedi-Moghaddam, A.; Rahmanian, E.; Naseri, N. Inkjet-Printing Technology for Supercapacitor Application: Current State and Perspectives. *ACS Appl. Mater. Interfaces* **2020**, *12*, 34487−34504.

(6) Li, L.; Zhang, Y.; Lu, H.; Wang, Y.; Xu, J.; Zhu, J.; Zhang, C.; Liu, T. Cryopolymerization Enables Anisotropic Polyaniline Hybrid

Hydrogels with Superelasticity and Highly Deformation-Tolerant Electrochemical Energy Storage. *Nat. Commun.* **2020**, *11*, No. 62.
(7) Lv, Z.; Luo, Y.; Tang, Y.; Wei, J.; Zhu, Z.; Zhou, X.; Li, W.; Zeng, Y.; Zhang, W.; Zhang, Y.; Qi, D.; Pan, S.; Loh, X. J.; Chen, X. Editable Supercapacitors with Customizable Stretchability Based on Mechanically Strengthened Ultralong MnO2 Nanowire Composite. *Adv. Mater.* **2018**, *30*, No. 1704531.
(8) Ye, T.; Wang, J.; Jiao, Y.; Li, L.; He, E.; Wang, L.; Li, Y.; Yun, Y.; Li, D.; Lu, J.; Chen, H.; Li, Q.; Li, F.; Gao, R.; Peng, H.; Zhang, Y. A Tissue-Like Soft All-Hydrogel Battery. *Adv. Mater.* **2022**, *34*, No. 2105120.
(9) Pan, S.; Zhang, F.; Cai, P.; Wang, M.; He, K.; Luo, Y.; Li, Z.; Chen, G.; Ji, S.; Liu, Z.; Loh, X. J.; Chen, X. Mechanically Interlocked Hydrogel−Elastomer Hybrids for on-Skin Electronics. *Adv. Funct. Mater.* **2020**, *30*, No. 1909540.
(10) Zhao, W.; Jiang, M.; Wang, W.; Liu, S.; Huang, W.; Zhao, Q. Flexible Transparent Supercapacitors: Materials and Devices. *Adv. Funct. Mater.* **2021**, *31*, No. 2009136.
(11) Chen, G.; Hu, O.; Lu, J.; Gu, J.; Chen, K.; Huang, J.; Hou, L.; Jiang, X. Highly Flexible and Adhesive Poly(Vinyl Alcohol)/Poly(Acrylic Amide-Co-2-Acrylamido-2-Methylpropane Sulfonic Acid)/Glycerin Hydrogel Electrolyte for Stretchable and Resumable Supercapacitor. *Chem. Eng. J.* **2021**, *425*, No. 131505.
(12) Wei, W.; Tang, Q.; Liu, T.; Xia, Y.; Yan, K.; Wang, D. Preparation and Properties of Polypyrrole/Polyamide 6 Nanocomposite Film with Core-Shell Architecture for the High-Performance Flexible Supercapacitor. *Compos. Commun.* **2020**, *22*, No. 100468.
(13) Wang, Y.; Chen, F.; Liu, Z.; Tang, Z.; Yang, Q.; Zhao, Y.; Du, S.; Chen, Q.; Zhi, C. A Highly Elastic and Reversibly Stretchable All-Polymer Supercapacitor. *Angew. Chem., Int. Ed.* **2019**, *58*, 15707−15711.
(14) Lai, F.; Yang, C.; Lian, R.; Chu, K.; Qin, J.; Zong, W.; Rao, D.; Hofkens, J.; Lu, X.; Liu, T. Three-Phase Boundary in Cross-Coupled Micro-Mesoporous Networks Enabling 3D-Printed and Ionogel-Based Quasi-Solid-State Micro-Supercapacitors. *Adv. Mater.* **2020**, *32*, No. 2002474.
(15) Gao, F.; Song, J.; Teng, H.; Luo, X.; Ma, M. All-Polymer Ultrathin Flexible Supercapacitors for Electronic Skin. *Chem. Eng. J.* **2021**, *405*, No. 126915.
(16) Keum, K.; Kim, J. W.; Hong, S. Y.; Son, J. G.; Lee, S. S.; Ha, J. S. Flexible/Stretchable Supercapacitors with Novel Functionality for Wearable Electronics. *Adv. Mater.* **2020**, *32*, No. 2002180.
(17) Guo, Y.; Zheng, K.; Wan, P. A Flexible Stretchable Hydrogel Electrolyte for Healable All-in-One Configured Supercapacitors. *Small* **2018**, *14*, No. 1704497.
(18) Wang, Y.; Ding, Y.; Guo, X.; Yu, G. Conductive Polymers for Stretchable Supercapacitors. *Nano Res.* **2019**, *12*, 1978−1987.
(19) Al-Ghaus, Z.; Akbarinejad, A.; Zhu, B.; Travas-Sejdic, J. Polyluminol-Polyoxometalate Hybrid Hydrogels as Flexible and Soft Supercapacitor Electrodes. *J. Mater. Chem. A* **2021**, *9*, 20783−20793.
(20) Wang, Y.; Wang, M.; Wang, P.; Zhou, W.; Chen, Z.; Gao, Q.; Shen, M.; Zhu, J. Urea-Treated Wet-Spun Pedot: Pss Fibers for Achieving High-Performance Wearable Supercapacitors. *Compos. Commun.* **2021**, *27*, No. 100885.
(21) Hu, G.; Zhang, X.; Liu, X.; Yu, J.; Ding, B. Strategies in Precursors and Post Treatments to Strengthen Carbon Nanofibers. *Adv. Fiber Mater.* **2020**, *2*, 46−63.
(22) Zhang, Q.; Hou, X.; Liu, X.; Xie, X.; Duan, L.; Lu, W.; Gao, G. Nucleotide-Tackified Organohydrogel Electrolyte for Environmentally Self-Adaptive Flexible Supercapacitor with Robust Electrolyte/Electrode Interface. *Small* **2021**, *17*, No. 2103091.
(23) Yang, J.; Yu, X.; Sun, X.; Kang, Q.; Zhu, L.; Qin, G.; Zhou, A.; Sun, G.; Chen, Q. Polyaniline-Decorated Supramolecular Hydrogel with Tough, Fatigue-Resistant, and Self-Healable Performances for All-in-One Flexible Supercapacitors. *ACS Appl. Mater. Interfaces* **2020**, *12*, 9736−9745.
(24) Qin, H.; Liu, P.; Chen, C.; Cong, H. P.; Yu, S. H. A Multi-Responsive Healable Supercapacitor. *Nat. Commun.* **2021**, *12*, No. 4297.
(25) Zhu, T.; Liu, S.; Wan, K.; Zhang, C.; Feng, Y.; Feng, W.; Liu, T. Fluorine and Nitrogen Dual-Doped Porous Carbon Nanosheet-Enabled Compact Electrode Structure for High Volumetric Energy Storage. *ACS Appl. Energy Mater.* **2020**, *3*, 4949−4957.
(26) Kunwar, R.; Krishnan, S. G.; Misnon, I. I.; Zabihi, F.; Yang, S.; Yang, C.-C.; Jose, R. Transformation of Supercapacitive Charge Storage Behaviour in a Multi Elemental Spinel Cumn2o4 Nanofibers with Alkaline and Neutral Electrolytes. *Adv. Fiber Mater.* **2021**, *3*, 265−274.
(27) Gan, D.; Huang, Z.; Wang, X.; Jiang, L.; Wang, C.; Zhu, M.; Ren, F.; Fang, L.; Wang, K.; Xie, C.; Lu, X. Graphene Oxide-Templated Conductive and Redox-Active Nanosheets Incorporated Hydrogels for Adhesive Bioelectronics. *Adv. Funct. Mater.* **2020**, *30*, No. 1907678.
(28) Cho, K. G.; Kim, H. S.; Jang, S. S.; Kyung, H.; Kang, M. S.; Lee, K. H.; Yoo, W. C. Optimizing Electrochemically Active Surfaces of Carbonaceous Electrodes for Ionogel Based Supercapacitors. *Adv. Funct. Mater.* **2020**, *30*, No. 2002053.
(29) Jin, X.; Sun, G.; Yang, H.; Zhang, G.; Xiao, Y.; Gao, J.; Zhang, Z.; Qu, L. A Graphene Oxide-Mediated Polyelectrolyte with High Ion-Conductivity for Highly Stretchable and Self-Healing All-Solid-State Supercapacitors. *J. Mater. Chem. A* **2018**, *6*, 19463−19469.
(30) Li, L.; Meng, J.; Zhang, M.; Liu, T.; Zhang, C. Recent Advances in Conductive Polymer Hydrogel Composites and Nanocomposites for Flexible Electrochemical Supercapacitors. *Chem. Commun.* **2021**, *58*, 185−207.
(31) Fang, L.; Cai, Z.; Ding, Z.; Chen, T.; Zhang, J.; Chen, F.; Shen, J.; Chen, F.; Li, R.; Zhou, X.; Xie, Z. Skin-Inspired Surface-Microstructured Tough Hydrogel Electrolytes for Stretchable Supercapacitors. *ACS Appl. Mater. Interfaces* **2019**, *11*, 21895−21903.
(32) Li, H.; Lv, T.; Sun, H.; Qian, G.; Li, N.; Yao, Y.; Chen, T. Ultrastretchable and Superior Healable Supercapacitors Based on a Double Cross-Linked Hydrogel Electrolyte. *Nat. Commun.* **2019**, *10*, No. 536.
(33) Shi, P.; Wang, Y.; Wan, K.; Zhang, C.; Liu, T. A Waterproof Ion-Conducting Fluorinated Elastomer with 6000% Stretchability, Superior Ionic Conductivity, and Harsh Environment Tolerance. *Adv. Funct. Mater.* **2022**, *32*, No. 2112293.
(34) Yu, Z.; Wu, P. Underwater Communication and Optical Camouflage Ionogels. *Adv. Mater.* **2021**, *33*, No. 2008479.
(35) Wang, Y.; Liu, Y.; Plamthottam, R.; Tebyetekerwa, M.; Xu, J.; Zhu, J.; Zhang, C.; Liu, T. Highly Stretchable and Reconfigurable Ionogels with Unprecedented Thermoplasticity and Ultrafast Self-Healability Enabled by Gradient-Responsive Networks. *Macromolecules* **2021**, *54*, 3832−3844.
(36) Zhao, Z.; Xia, K.; Hou, Y.; Zhang, Q.; Ye, Z.; Lu, J. Designing Flexible, Smart and Self-Sustainable Supercapacitors for Portable/Wearable Electronics: From Conductive Polymers. *Chem. Soc. Rev.* **2021**, *50*, 12702−12743.
(37) Wang, Y.; Tebyetekerwa, M.; Liu, Y.; Wang, M.; Zhu, J.; Xu, J.; Zhang, C.; Liu, T. Extremely Stretchable and Healable Ionic Conductive Hydrogels Fabricated by Surface Competitive Coordination for Human-Motion Detection. *Chem. Eng. J.* **2021**, *420*, No. 127637.
(38) Chen, M.; Chen, J.; Zhou, W.; Xu, J.; Wong, C.-P. High-Performance Flexible and Self-Healable Quasi-Solid-State Zinc-Ion Hybrid Supercapacitor Based on Borax-Crosslinked Polyvinyl Alcohol/Nanocellulose Hydrogel Electrolyte. *J. Mater. Chem. A* **2019**, *7*, 26524−26532.
(39) Yuan, W.-Q.; Liu, G.-L.; Huang, C.; Li, Y.-D.; Zeng, J.-B. Highly Stretchable, Recyclable, and Fast Room Temperature Self-Healable Biobased Elastomers Using Polycondensation. *Macromolecules* **2020**, *53*, 9847−9858.
(40) Liu, S.; Wan, K.; Zhang, C.; Liu, T. Polyaniline-Decorated 3d Carbon Porous Network with Excellent Electrolyte Wettability and

https://doi.org/10.1021/acsami.2c13829
ACS Appl. Mater. Interfaces 2022, 14, 45910−45920

High Energy Density for Supercapacitors. *Compos. Commun.* **2021**, *24*, No. 100610.
(41) Zhang, M. Y.; Song, Y.; Yang, D.; Qin, Z.; Guo, D.; Bian, L. J.; Sang, X. G.; Sun, X.; Liu, X. X. Redox Poly-Counterion Doped Conducting Polymers for Pseudocapacitive Energy Storage. *Adv. Funct. Mater.* **2021**, *31*, No. 2006203.
(42) Ji, S.; Yang, J.; Cao, J.; Zhao, X.; Mohammed, M. A.; He, P.; Dryfe, R. A. W.; Kinloch, I. A. A Universal Electrolyte Formulation for the Electrodeposition of Pristine Carbon and Polypyrrole Composites for Supercapacitors. *ACS Appl. Mater. Interfaces* **2020**, *12*, 13386−13399.
(43) Zhu, T.; Feng, Q.; Liu, S.; Zhang, C. Metallogel-Derived 3d Porous Carbon Nanosheet Composites as an Electrocatalyst for Oxygen Reduction Reaction. *Compos. Commun.* **2020**, *20*, No. 100376.
(44) Stoller, M. D.; Ruoff, R. S. Best Practice Methods for Determining an Electrode Material's Performance for Ultracapacitors. *Energy Environ. Sci.* **2010**, *3*, 1294.
(45) Wang, T.; Wang, Y.; Lei, J.; Chen, K. J.; Wang, H. Electrochemically Induced Surface Reconstruction of Ni-Co Oxide Nanosheet Arrays for Hybrid Supercapacitors. *Exploration* **2021**, *1*, No. 20210178.
(46) Eftekhari, A. The Mechanism of Ultrafast Supercapacitors. *J. Mater. Chem. A* **2018**, *6*, 2866−2876.
(47) Zong, W.; Guo, H.; Ouyang, Y.; Mo, L.; Zhou, C.; Chao, G.; Hofkens, J.; Xu, Y.; Wang, W.; Miao, Y. E.; He, G.; Parkin, I. P.; Lai, F.; Liu, T. Topochemistry-Driven Synthesis of Transition-Metal Selenides with Weakened Van Der Waals Force to Enable 3d-Printed Na-Ion Hybrid Capacitors. *Adv. Funct. Mater.* **2022**, *32*, No. 2110016.
(48) Wang, Z.; Pan, Q. An Omni-Healable Supercapacitor Integrated in Dynamically Cross-Linked Polymer Networks. *Adv. Funct. Mater.* **2017**, *27*, No. 1700690.
(49) Wang, L.; Zhang, C.; Jiao, X.; Yuan, Z. Polypyrrole-Based Hybrid Nanostructures Grown on Textile for Wearable Supercapacitors. *Nano Res.* **2019**, *12*, 1129−1137.
(50) Wang, Q.; Wang, X.; Wan, F.; Chen, K.; Niu, Z.; Chen, J. An All-Freeze-Casting Strategy to Design Typographical Supercapacitors with Integrated Architectures. *Small* **2018**, *14*, No. 1800280.

Recommended by ACS

Water-Enhanced and Remote Self-Healing Elastomers in Various Harsh Environments
Peng Zhao, Huaping Xu, *et al.*
JUNE 02, 2022
ACS APPLIED MATERIALS & INTERFACES
READ

Noncovalent Assembly Enabled Strong yet Tough Materials with Room-Temperature Malleability and Healability
Xin Yang, Xinxing Zhang, *et al.*
AUGUST 05, 2022
ACS NANO
READ

High Toughness Polyurethane toward Artificial Muscles, Tuned by Mixing Dynamic Hard Domains
Qiqi Qu, Hua Wang, *et al.*
AUGUST 26, 2021
MACROMOLECULES
READ

Rationally Constructed Surface Energy and Dynamic Hard Domains Balance Mechanical Strength and Self-Healing Efficiency of Energetic Linear Polymer Materials
Shanjun Ding, Yunjun Luo, *et al.*
JULY 19, 2021
LANGMUIR
READ

Get More Suggestions >

https://doi.org/10.1021/acsami.2c13829
ACS Appl. Mater. Interfaces 2022, 14, 45910−45920